Coupling analysis of high Q resonators in add-drop configuration through cavity ringdown spectroscopy

Gabriele Frigenti, Mojtaba Arjmand, Andrea Barucci, Francesco Baldini, Simone Berneschi, Daniele Farnesi, Mariagiovanna Gianfreda, Stefano Pelli, Silvia Soria, A Aray, et al.

HAL Id: hal-01940112

https://hal.science/hal-01940112

Submitted on 12 Mar 2020

Coupling analysis of high Q resonators in add-drop configuration through cavity ringdown spectroscopy

G Frigenti[1,2,6] , M Arjmand[3] , A Barucci[1], F Baldini[1], S Berneschi[1],
D Farnesi[1], M Gianfreda[4], S Pelli[1], S Soria[1], A Aray[3], Y Dumeige[5] ,
P Féron[5] and G Nunzi Conti[1]

[1]IFAC-CNR, Institute of Applied Physics 'Nello Carrara', National Research Council, Via Madonna del Piano 10, I-50019 Sesto Fiorentino (FI), Italy
[2]Laboratorio Europeo di Spettroscopia (LENS), Università degli Studi di Firenze via Nello Carrara 1, 150019 Sesto F.no, Firenze, Italy
[3]Optics and Laser Sciences & Technology Research Center, Malek-Ashtar University of Technology, 83145-13115, Shahin-Shahr, Isfahan, Iran
[4]Centro Fermi - Museo Storico della Fisica e Centro Studi e Ricerche 'Enrico Fermi', Piazza del Viminale 1, I-00184 Roma, Italy
[5]FOTON (CNRS - UMR 6082), Université de Rennes 1, ENSSAT, 6 rue de Kerampont, F-22300 Lannion, France

E-mail: g.frigenti@ifac.cnr.it

Abstract

An original method able to fully characterize high-Q resonators in an add-drop configuration has been implemented. The method is based on the study of two cavity ringdown (CRD) signals, which are produced at the transmission and drop ports by wavelength sweeping a resonance in a time interval comparable with the photon cavity lifetime. All the resonator parameters can be assessed with a single set of simultaneous measurements. We first developed a model describing the two CRD output signals and a fitting program able to deduce the key parameters from the measured profiles. We successfully validated the model with an experiment based on a fiber ring resonator of known characteristics. Finally, we characterized a high-Q, home-made, MgF_2 whispering gallery mode disk resonator in the add-drop configuration, assessing its intrinsic and coupling parameters.

Keywords: optical resonators, microcavities, whispering gallery mode resonators, fiber optics, cavity ringdown spectroscopy

1. Introduction

Whispering gallery mode (WGM) resonators are a family of resonators with curved dielectric interfaces with cylindrical symmetry that allow guiding light in two directions by total internal reflection on a quasi-circular path. There are many possible shapes for them, like rings, toroids, spheres and disks, and, if they are made in low loss materials and have a small footprint (few millimetres or below), they can share the

common feature of having very high quality factors and little modal volumes. These characteristics make them interesting for fundamental studies, for instance, in non-linear optics, and for practical applications, like sensing and optical processing. In all cases, being able to characterise the intrinsic properties of the WGM resonator and its interactions with the input-output couplers becomes an important requirement.

The general procedure to couple light to a WGM resonator is to use the evanescent tail of a bus waveguide or a prism, which has to be phase matched and partially overlapped to the WGM [1].

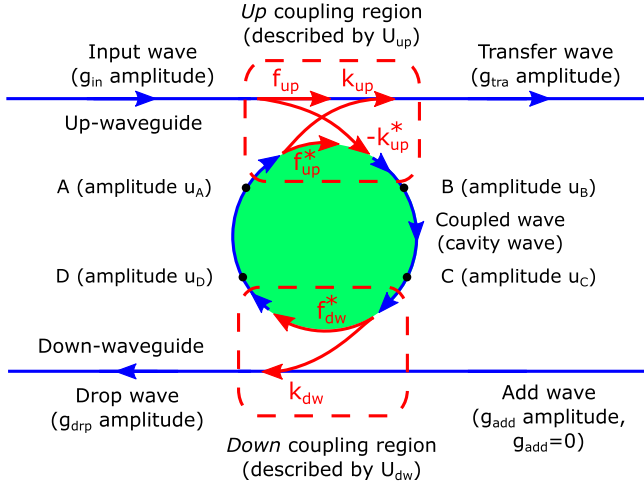[6] Author to whom any correspondence should be addressed.

Figure 1. Sketch of the add-drop configuration showing the nomenclature used in section 2.1: the red arrows represent the coupling between the resonator and the two waveguides, while the red letters close to the arrows show the matrix elements of U_{up} and U_{down} that relates the g's to the u's (see (3) and (4)). The size of the coupling zones is exaggerated for the sake of clarity.

In particular, we realise an *add-drop configuration* by coupling the WGM resonator to two tapered fibers, therefore having a two coupler and a four port device. The add-drop configuration is very important for a number of studies based on ultra-high-Q WGM microresonators that have recently gained great interest, including, for instance, the implementation of innovative compact Kerr frequency combs [2–5], the generation of non linear parametric [6, 7] and non-parametric [8, 9] oscillations, the stabilization of semiconductor lasers operating in the resonators transparent wavelength range [10–12], or the mode-locking of fast pulsed lasers [13]. In these experiments, where the frequency conversion through non-linear effects (as well as laser oscillations [14]) is accomplished within the resonators, the add-drop configuration allows us to efficiently collect the signal through the drop channel, while keeping the residual pump on the transfer channel.

The configuration investigated in this work is also very useful for practical applications in which the add-drop configuration is the core optical unit for devices like innovative ultra-compact RF optoelectronic oscillators [3, 15, 16] or ultra-narrow filters [17] and non-linear switches [18–21].

Indeed, being able to completely characterize such WGM resonator based systems is a key step for understanding basic studies as well as for implementing and optimising the performances of new devices.

The main motivation for this work has been to implement an original technique based on *cavity ringdown spectroscopy* (CRDS) which is capable of uniquely assessing the various parameters of a WGM resonator in the add-drop configuration by using a single set of measurements. CRD based techniques may, similar to cavity ringup (CRU) [22], allow us to assess intrinsic fundamental properties of the resonators, thanks to their high speed processing capabilities [23, 24].

2. Model

The sketch shown in figure 1 represents the typical two-waveguides configuration, or add-drop configuration, where a resonator, depicted as a green disk, is coupled to two waveguides, depicted as blue straight lines in its proximity. The coupling between these elements is graphically represented by two red dashed rectangles and allows light exchange between the waveguides and the resonator. Finally, a set of arrows depicts the direction of light propagation, with the output branches of the two waveguides named the *transfer channel* and *drop channel*.

The monochromatic input wave is assumed to be linearly scanned in frequency: depending on the value of the *frequency scan speed* V_s, the output traces can be very different.

If V_s is below a threshold scanning speed V_s^{thr}, the resonator excitation is *stationary* (or adiabatic), and the transmission spectrum of the resonator is formed by a series of dips for the transfer channel and a series of spikes for the drop channel (section 2.1). Instead, if $V_s > V_s^{thr}$, the traces feature oscillations of decreasing amplitude and period (*cavity ringdown regime*, section 2.2).

The value of V_s^{thr} can be intuitively estimated as the scanning velocity that produces a resonance crossing time FWHM/V_s^{thr} equal to the photon lifetime inside the resonator (τ_{tot}), i.e. [25]

$$V_s^{thr} = \frac{2}{\pi \tau_{tot}^2}.$$

In the following, we resume the results and the limits related to stationary regime measurements (section 2.1) and then describe the model developed to predict the transfer and drop signals in the CRD regime (section 2.2). In both cases, we assume that only one mode is excited in both the resonator and the waveguide, ignoring multimode propagation [26]. However, we do not make any assumptions on the specific features of the resonator or the waveguide, so that the model can be general and can describe any type of waveguide-resonator combination.

2.1. Stationary profiles

Following the coupling matrix formalism described in [27], we introduce the two unitary matrices U_{up} and U_{down} to mathematically describe the coupling between the resonator and the waveguides when $V_s < V_s^{thr}$:

$$U_{up} = \begin{pmatrix} f_{up} & k_{up} \\ -k_{up}^* & f_{up}^* \end{pmatrix}$$

$$U_{down} = \begin{pmatrix} f_{dw} & k_{dw} \\ -k_{dw}^* & f_{dw}^* \end{pmatrix}$$

$$f_{up} = |f_{up}|\, e^{j\phi_{up}}$$

$$f_{dw} = |f_{dw}|\, e^{j\phi_{dw}}$$

$$|f_{up}|^2 + |k_{up}|^2 = 1 \tag{1}$$

$$|f_{down}|^2 + |k_{down}|^2 = 1, \tag{2}$$

where k_up and k_down are the coupling factors of the up-waveguide and of the down-waveguide respectively, while f_up and f_down are the corresponding transmission factors. The complex exponential form for f_up and f_down allows us to write some equations in a more compact form (e.g. (7) and (8)), while the conditions (1) and (2) are a consequence of the *lossless coupling hypothesis*, which states that light entering the coupling region can only be transmitted to the waveguide or moved to the resonator, and not be lost in a third channel. The coupling factors are proportional to the overlap integral between the mode of the resonator and the corresponding waveguide modes, and their squared moduli $|k_\text{up}|^2$ and $|k_\text{down}|^2$ define the fractions of optical power exchanged between these elements [28].

The matrices U_up and U_{dw} connect the complex amplitudes g_{in}, g_{tra}, g_{drp} and g_{add}, used to describe light propagation through the waveguides modes, and the complex amplitudes u_A, u_B, u_C and u_D, used to describe light propagation through the resonator mode. By computing the squared modulus of these complex amplitudes, it is possible to deduce the optical power in various points of the light path. Since we are not injecting light through the add channel, we set $g_{add} = 0$. Mathematically, the connection between the g's and u's is made through the following:

$$\begin{pmatrix} g_{tra} \\ u_B \end{pmatrix} = U_\text{up} \begin{pmatrix} g_{in} \\ u_A \end{pmatrix} \tag{3}$$

$$\begin{pmatrix} g_{drp} \\ u_D \end{pmatrix} = U_\text{down} \begin{pmatrix} g_{add} \\ u_C \end{pmatrix}, \tag{4}$$

which can be translated into a system of equations by applying the matrix product.

To complete the system resulting from (3) and (4), we have to set the *propagation conditions*, which relate the amplitudes of the u's inside the resonator (see figure 1):

$$u_C = \sqrt{\alpha} \; e^{j\omega(\tau_\text{rnd}/2)} \, u_B \tag{5}$$

$$u_A = \sqrt{\alpha} \; e^{j\omega(\tau_\text{rnd}/2)} \, u_D, \tag{6}$$

where τ_rnd is the round trip time and α is the round trip transmission factor of the resonator mode, which can be deduced by the fraction of optical power lost in a round trip (η^2) [29]. The expression for these quantities is:

$$\tau_\text{rnd} = \frac{n\,L}{c}$$

$$\alpha = \sqrt{1 - \eta^2},$$

where L is the resonator length and n is the material refractive index. In the ideal case of a resonator with no losses, we have $\eta^2 = 0$ and $\alpha = 1$. Also, in (5) and (6), we adopted the usual notation for the angular frequencies: $\omega = 2\pi\,\nu = 2\pi\,c/\lambda$, since $\lambda\nu = c$.

The system originating from the combination of (3)–(6) is solved by fixing g_{in} as an independent quantity and writing the other amplitudes in terms of g_{in}. Then, we can compute $s_\text{tra} = |g_{tra}/g_{in}|^2$ and $s_\text{drp} = |g_{drp}/g_{in}|^2$, which represent the optical powers of the transfer wave and of the drop wave with

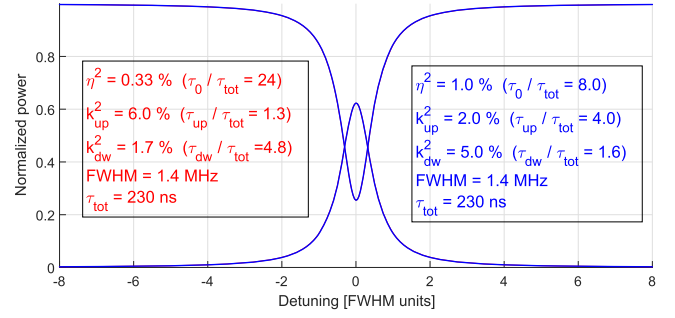**Figure 2.** Plots of s_tra and s_drp versus $x = (\nu - \nu_0)/\text{FWHM}$ with parameter values typical for a fiber ring resonator. The two parameter sets chosen for this figure highlight the limits of stationary regime measurements: in fact, the two sets, albeit different, produce perfectly overlapping profiles, making impossible to distinguish between them. In this plot, the blue curves are in the foreground and hide the red ones.

respect to the laser input power:

$$s_\text{tra} = \frac{|f_\text{up}|^2 + |f_\text{down}|^2\,\alpha^2 - 2T\cos(\omega\tau_\text{rnd} - \phi_\text{up} - \phi_\text{dw})}{1 + T^2 - 2T\cos(\omega\tau_\text{rnd} - \phi_\text{up} - \phi_\text{dw})} \tag{7}$$

$$s_\text{drp} = \frac{|k_\text{up}|^2\,|k_\text{down}|^2\,\alpha}{1 + T^2 - 2T\cos(\omega\tau_\text{rnd} - \phi_\text{up} - \phi_\text{dw})}, \tag{8}$$

where $T = |f_\text{up}||f_\text{down}|\,\alpha$.

By plotting (7) and (8) as functions of λ or ν, we get a dip on s_tra and a spike on s_drp whenever $\omega\tau_\text{rnd} - \phi_\text{up} - \phi_\text{dw} = 0$. The resonances are identical to each other, presenting a quasi-Lorentzian shape, and are separated by the *free spectral range* $\text{FSR} = 1/\tau_\text{rnd}$. Figure 2 shows the resonance profile of a fiber ring resonator similar to the one studied in section 3, assuming $\phi_\text{up} = \phi_\text{dw} = 0$ and setting k_up, k_down and η to typical values for this kind of resonator. Instead of ν, we adopted the normalized detuning from resonance $x = (\nu - \nu_0)/\text{FWHM}$ as the abscissa, where FWHM is the full width half maximum of the profiles and ν_0 is the resonance frequency. From (7) and (8), we can obtain the analytical expression for the FWHM as shown in (15).

Since the resonances are identical and the data analysis focuses on the study of the resonance shape, it is common to recast (7) and (8) in a different form through a Taylor expansion around a resonance frequency ν_0, assuming small intrinsic losses and small coupling losses ($\eta^2 \ll 1$, $|k_\text{up}|^2 \ll 1$, $|k_\text{down}|^2 \ll 1$). By doing so, we obtain the following expressions

$$s_\text{tra} = \frac{\left(\frac{1}{\tau_\text{up}} - \frac{1}{\tau_\text{down}} - \frac{1}{\tau_0}\right)^2 + 4\pi^2(\nu - \nu_0)^2}{\left(\frac{1}{\tau_\text{up}} + \frac{1}{\tau_\text{down}} + \frac{1}{\tau_0}\right)^2 + 4\pi^2(\nu - \nu_0)^2} \tag{9}$$

$$s_\text{drp} = \frac{\frac{4}{\tau_\text{up}\tau_\text{down}}}{\left(\frac{1}{\tau_\text{up}} + \frac{1}{\tau_\text{down}} + \frac{1}{\tau_0}\right)^2 + 4\pi^2(\nu - \nu_0)^2}, \tag{10}$$

where the lifetimes τ_0, τ_up and τ_down are defined as

$$\tau_0 = \frac{2\tau_{\text{rnd}}}{\eta^2} \tag{11}$$

$$\tau_{\text{up}} = \frac{2\tau_{\text{rnd}}}{|k_{\text{up}}|^2} \tag{12}$$

$$\tau_{\text{down}} = \frac{2\tau_{\text{rnd}}}{|k_{\text{down}}|^2}. \tag{13}$$

Physically, the intrinsic lifetime τ_0 is the average time that one photon spends inside the resonator before being lost due to intrinsic losses; τ_{up} and τ_{down}, instead, quantify the average time inside the resonator before being moved to the up-waveguide or the down-waveguide, respectively. To mathematically describe the add-drop system, it is possible to equivalently use the triplet $(\eta^2, |k_{\text{up}}|^2, |k_{\text{down}}|^2)$ or the triplet $(\tau_0, \tau_{\text{up}}, \tau_{\text{down}})$, since they are related through equations (11)–(13).

Additionally, we can define a total lifetime τ_{tot} to take into account all the loss mechanisms by combining the previous lifetimes:

$$\tau_{\text{tot}} = \left(\frac{1}{\tau_0} + \frac{1}{\tau_{\text{up}}} + \frac{1}{\tau_{\text{down}}} \right)^{-1}. \tag{14}$$

The functions s_{tra} and s_{drp} (equations (9) and (10)) show symmetry under the exchange of the lifetimes: for the transfer channel, we notice the exchange symmetry $\tau_0 \leftrightarrow \tau_{\text{down}}$ and $1/\tau_{\text{up}} \leftrightarrow 1/\tau_0 + 1/\tau_{\text{down}}$, while for the drop channel, we notice the exchange symmetry $\tau_{\text{up}} \leftrightarrow \tau_{\text{down}}$. As a practical consequence, these symmetries lead to the possibility for different parameter sets to have identical transfer and drop profiles, leading to an ambiguous estimation of the parameters.

In the end, with a slow scan, we cannot unambiguously assign the parameter set $(\tau_0, \tau_{\text{up}}, \tau_{\text{down}})$ and we can only access limited information regarding the main parameters of a resonator, like the FWHM, the *finesse* $\mathcal{F}$, the *quality factor* Q_{tot}, the *cavity build-up factor* C_{b} and the *drop efficiency D*, which is the maximum power ratio transmitted to the drop channel. The expressions of these parameters are deduced through the analytical formulas for transfer and drop profiles, shown in equations (7)–(10):

$$\text{FWHM} = \frac{1}{\pi\tau_{\text{rnd}}} \sqrt{\frac{(1-T)^2}{T}} = \frac{1}{\pi\,\tau_{\text{tot}}} \tag{15}$$

$$\mathcal{F} = \frac{\text{FSR}}{\text{FWHM}} = \pi\sqrt{\frac{T}{(1-T)^2}} = \pi\frac{\tau_{\text{tot}}}{\tau_{\text{rnd}}} \tag{16}$$

$$Q_{\text{tot}} = \frac{\nu_0}{\text{FWHM}} = \pi\nu_0\tau_{\text{tot}} \tag{17}$$

$$C_{\text{b}} = \max(s_{\text{cav}}) = \frac{|k_{\text{up}}|^2}{(1-T)^2} \tag{18}$$

$$D = \max(s_{\text{drp}}) = \frac{\alpha\,|k_{\text{up}}|^2|k_{\text{down}}|^2}{(1-T)^2} \tag{19}$$

From data fitting, we can only deduce the total lifetime τ_{tot}, since this parameter is symmetric with respect to all three τ's, and we can only compute $\mathcal{F}$, Q_{tot} and FWHM. The cavity build up factor C_{b}, which is a key value in non-linear optics applications, remains unknown. To achieve a complete characterisation of the resonator, we have to study the CRD regime.

2.2. CRD profiles

The theory describing the dynamic regime, or CRD regime, is formulated in the time domain and is based on the coupled mode theory described in [30] and extended in [25], which focuses on the energy exchange between the resonator and the waveguides. We use the complex amplitudes $u(t)$, $g_{\text{tra}}(t)$ and $g_{\text{drp}}(t)$ to describe the optical energy stored inside the resonator mode (equal to $|u(t)|^2$) and the optical powers flowing in the waveguides during the fast frequency scan (equal to $|g_{\text{tra}}(t)|^2$ and $|g_{\text{drp}}(t)|^2$).

The differential equations based on the coupled mode theory, describing an add-drop system when no add wave is injected, are:

$$\frac{du}{dt} = \left(j\omega_0 - \frac{1}{\tau_{\text{tot}}} \right)u(t) + \sqrt{\frac{2}{\tau_{\text{up}}}}\,g_{\text{in}}(t) \tag{20}$$

$$g_{\text{tra}} = -g_{\text{in}} + \sqrt{\frac{2}{\tau_{\text{up}}}}\,u(t) \tag{21}$$

$$g_{\text{drp}} = \sqrt{\frac{2}{\tau_{\text{down}}}}\,u(t). \tag{22}$$

To solve equations (20)–(22), we fix the analytical structure of the source term $g_{\text{in}}(t)$ as follows:

$$g_{\text{in}}(t) = g_0\,e^{j\phi(t)} \qquad \text{with} \qquad \phi(t) = \omega(t)\,t,$$

where $\phi(t)$ is the phase of the laser wave and $|g_0|^2$ is its optical power. Since we assume a constant scanning speed V_{s} and a non-resonant initial frequency ν_{i}, we can write $\omega(t)$ and the instantaneous laser frequency $\nu(t)$ as follows [25]:

$$\omega(t) = 2\pi\left(\nu_{\text{i}} + \frac{V_{\text{s}}}{2}\,t\right)$$

$$\nu(t) = \frac{1}{2\pi}\frac{d\phi}{dt} = \nu_{\text{i}} + V_{\text{s}}t, \tag{23}$$

obtaining in the end the following expression for $g_{\text{in}}(t)$:

$$g_{\text{in}}(t) = g_0\exp(j(2\pi\,\nu_{\text{i}}\,t + \pi\,V_{\text{s}}\,t^2)).$$

With a source term of this form, equation (20) can be integrated using an harmonic oscillator model for $u(t)$, which leads to the following solution [25]:

$$u(t) = \sqrt{\frac{2}{\tau_{\text{up}}}}\,g_0\exp\left(j\omega_0 t - \frac{t}{\tau_{\text{tot}}} \right)$$

$$\times \left[f(t) - f(0) + \frac{1}{j\delta\omega_{\text{i}} + 1/\tau_{\text{tot}}} \right]$$

where the function $f(t)$ is an auxiliary function defined through the complex error function erf(z):
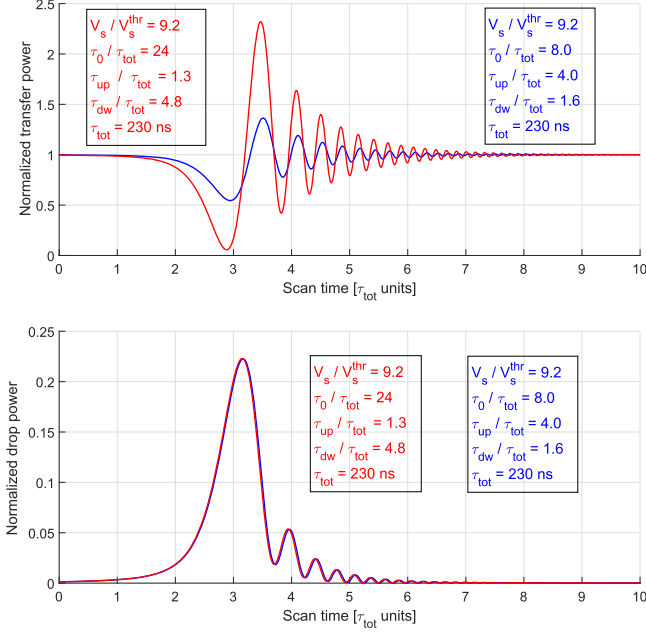
4

Figure 3. Cavity ringdown profiles corresponding to the same parameter sets of figure 2, which produce identical stationary profiles. In this regime, the profiles are easily distinguishable.

$$f(t) = -\sqrt{\frac{j\pi}{2W_s}} \, \exp\left(\frac{-j(\delta\omega_i - j/\tau_{tot})^2}{2W_s}\right)$$
$$\times \, \text{erf}\left(\frac{j/\tau_{tot} - \delta\omega_i - W_s \, t}{\sqrt{2jW_s}}\right).$$

In both equations, we define the initial detuning from resonance as $\nu_i - \nu_0 = \delta\nu_i$, its angular counterpart as $\delta\omega_i = 2\pi(\nu_i - \nu_0)$ and the angular scanning speed as $W_s = 2\pi V_s$.

We can now compute the normalized power profiles $s_{tra} = |g_{tra}/g_0|^2$ and $s_{drp} = |g_{drp}/g_0|^2$ substituting $u(t)$ into (21) and (22):

$$s_{tra}(t) = \left| -\exp\left(j\left(\delta\omega_i \, t + \frac{W_s}{2} \, t^2\right)\right) + \frac{2\,e^{-t/\tau_{tot}}}{\tau_{up}}\right.$$
$$\left. \times \left(f(t) - f(0) + \frac{1}{j\,\delta\omega_i + 1/\tau_{tot}}\right)\right|^2 \quad (24)$$

$$s_{drp}(t) = \left| \sqrt{\frac{4}{\tau_{down}\tau_{up}}} \, e^{-t/\tau_{tot}}\right.$$
$$\left. \times \left(f(t) - f(0) + \frac{1}{j\,\delta\omega_i + 1/\tau_{tot}}\right)\right|^2. \quad (25)$$

Typical examples of s_{tra} and s_{drp} profiles are reported in figure 3, where we adopted normalized time units for the abscissa ($x = t/\tau_{tot}$), instead of the absolute time t. Also, the figure shows the key feature of the dynamic regime, which is the possibility to distinguish between different parameter sets producing identical stationary profiles (the common stationary profile is the one reported in figure 2).

By simultaneously recording the transfer and the drop signals, and then fitting these data with the functions reported
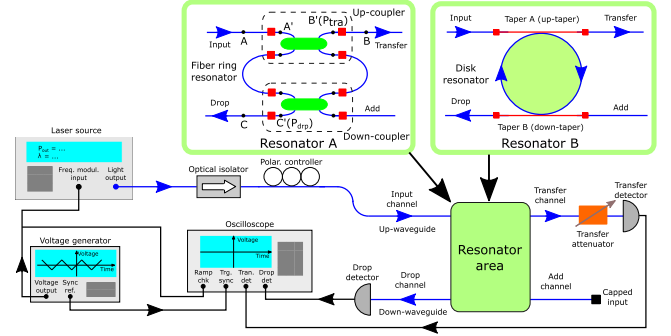

Figure 4. Sketch of the setup used to study the fiber ring resonator (resonator A, section 3) and the WGM resonator (resonator B, section 4).

in (24) and (25), it is possible to uniquely obtain the lifetimes τ_0, τ_{up} and τ_{down}, completely characterising the system with one set of measurements. The fitting procedure is divided into two steps: firstly, we fit the transfer signal to obtain the value of τ_{up}, which appears in s_{tra} in a non-symmetric way under the exchange with τ_0 and τ_{down}; then, while locking τ_{up} to the value resulting from the first fit, we perform a second fit on the drop channel to determine the values of τ_0 and τ_{down}, since they appear in a non-symmetric way in s_{drp}.

From the three lifetimes τ_0, τ_{up} and τ_{down}, it is possible to deduce α, k_{up} and k_{down} by inversion of equations (11)–(13), and it is also possible to compute the parameters listed in equations (15)–(19). In addition, it is possible to compute three auxiliary quality factors Q_0, Q_{up} and Q_{down}, associated with the intrinsic losses, the up-coupling losses and the down-coupling losses, respectively, defined as in [30]:

$$Q_0 = \pi \, \nu_0 \, \tau_0 \quad (26)$$

$$Q_{up} = \pi \, \nu_0 \, \tau_{up} \quad (27)$$

$$Q_{down} = \pi \, \nu_0 \, \tau_{down}, \quad (28)$$

where ν_0 is the frequency of the resonance.

3. Experiment on fiber ring resonator

In this section, we validate the theoretical model of section 2 through an experiment on a fiber ring resonator.

3.1. Setup description and data acquisition

The experimental setup shown in figure 4 was designed to be versatile, allowing the characterisation of both a fiber ring resonator (resonator A) or a WGM resonator using tapered fibers as coupling elements (resonator B). In this section, we are interested in the fiber ring resonator, which was made by splicing a pair of 2-by-2 fiber couplers with fibers having a core index $n = 1.47$ and total length $L = 3.52$ m, giving a round trip time $\tau_{rnd} \approx 17$ ns and a free spectral range FSR ≈ 58 MHz.

Before the experiment, we characterised the two couplers (labelled as *up-coupler* and *down-coupler* in figure 4) in an open loop configuration by measuring their coupling constant $|k|^2$ and their intrinsic losses (commonly called *excess losses*) using an

infrared power meter (Ando AQ2742). These measurements confirmed the manufacturer specifications, giving $|k_{\text{up}}|^2 \approx 5\%$ and $|k_{\text{down}}|^2 \approx 1\%$. Also, to take into account the excess losses, we modelled the real coupler as shown in figure 4, using the combination of an ideal coupler (green ellipsis) and four identical lossy elements (red squares) with a transmission factor γ. The values of $\gamma_{\text{up}} \approx 99\%$ and $\gamma_{\text{down}} \approx 98\%$ have been deduced from the measured intrinsic losses.

The resonator was excited by a CW infrared laser source (NetTest Tunics) working in the spectral range from 1500 nm to 1640 nm with a reported linewidth of 150 KHz, and using a modified Littman-Metcalf configuration to achieve a fine wavelength selection through a voltage function generator. In our case, we applied a triangular shaped ramp, which allowed us to cover a spectral interval close to 3 GHz ($\approx$25 pm). After the laser source, we placed an optical isolator and a polarisation controller. In fact, due to mechanical stress inside the fiber ring, the resonance frequencies ν_ℓ of the two polarisation families did not coincide, producing a splitting between the two families. Apart from this frequency shift, TE and TM resonances exhibited the same profiles and were not distinguishable.

The two output lines of the ring, which defined the transfer channel and drop channel, were connected to two fast amplified InGaAs detectors (Thorlabs PDA8GS, bandwidth: 9.5 GHz, maximum power: 1 mW), while the second input line, defining the add channel, was not used. An attenuator with an attenuation factor a_{tra} protects the detector on the transfer channel. The signals from the detectors were collected with a digital oscilloscope (Tektronix DPO 7104, bandwidth: 1 GHz).

To compare the experimental data with the theory developed in section 2, it is necessary to deduce a normalized power profile for both transfer and drop channels, starting from the recorded data. In particular, we want to estimate the normalized power at points B$'$ and C$'$ of figure 4, which are the actual output signals of the add-drop resonator.

We start by converting the voltage traces V_{tra} and V_{drp} into the detected power traces $P_{\text{det,tra}}$ and $P_{\text{det,drp}}$ applying the calibration lines of the detectors

$$P = \frac{V - q}{m},$$

where m and q are the sensitivity (in mV/μW) and the offset (in mV), respectively. Then, taking into account the attenuation factor a_{tra} and the excess losses of the couplers, it is possible to deduce the power profiles P_{tra} (equal to $P_{\text{B}'}$) and P_{drp} (equal to $P_{\text{C}'}$):

$$P_{\text{tra}}(t) = P_{\text{det,tra}}(t) \frac{a_{\text{tra}}}{\gamma_{\text{up}}} = \frac{V_{\text{tra}}(t) - q_{\text{tra}}}{m_{\text{tra}}} \frac{a_{\text{tra}}}{\gamma_{\text{up}}}$$

$$P_{\text{drp}}(t) = P_{\text{det,drp}}(t) \frac{1}{\gamma_{\text{down}}} = \frac{V_{\text{drp}}(t) - q_{\text{drp}}}{m_{\text{drp}}} \frac{1}{\gamma_{\text{down}}},$$

where t stands for the acquisition times. The last step consists in the normalisation of P_{tra} and P_{drp} to the input power of the ring P_{in}, which is marked as P_{A}' in figure 4. This input power is deduced by noticing that, for high finesse resonators, we can compute P_{in} as the mean value of P_{tra} when the laser is off-resonance.

In the end, the normalized power profiles n_{tra} and n_{drp} are computed as

$$n_{\text{tra}}(t) = \frac{P_{\text{tra}}(t)}{P_{\text{in}}} \tag{29}$$

$$n_{\text{drp}}(t) = \frac{P_{\text{drp}}(t)}{P_{\text{in}}}. \tag{30}$$

These curves are the experimental counterparts of the functions s_{tra} and s_{drp} deduced by the theory of section 2 and can be used to characterise the resonator through the data fitting method described in the following subsections.

3.2. Stationary analysis

Because of the exchange symmetry described in section 2.1, stationary profiles cannot be used to deduce the single τ's, but can be used to deuced the total lifetime τ_{tot}.

To evaluate τ_{tot}, we perform a least-squares fitting on the experimental profiles and then compute τ_{tot} via (14). To do so, we start by replacing ν in (9) and (10) with $\nu(t)$ from (23), obtaining two functions $s_{\text{fit}}^{\text{tra}}$ and $s_{\text{fit}}^{\text{drp}}$ depending on the variables $(t; \tau_{\text{up}}, \tau_{\text{down}}, \tau_0, \delta_i)$:

$$s_{\text{fit}}^{\text{tra}} = \frac{\left(\frac{1}{\tau_{\text{up}}} - \frac{1}{\tau_{\text{down}}} - \frac{1}{\tau_0}\right)^2 + 4\pi^2(\delta_i + V_s t)^2}{\left(\frac{1}{\tau_{\text{up}}} + \frac{1}{\tau_{\text{down}}} + \frac{1}{\tau_0}\right)^2 + 4\pi^2(\delta_i + V_s t)^2}$$

$$s_{\text{fit}}^{\text{drp}} = \frac{\frac{4}{\tau_{\text{up}}\tau_{\text{down}}}}{\left(\frac{1}{\tau_{\text{up}}} + \frac{1}{\tau_{\text{down}}} + \frac{1}{\tau_0}\right)^2 + 4\pi^2(\delta_i + V_s t)^2},$$

where $\delta_i = \nu_i - \nu_0$ is again the initial detuning from resonance.

We then define the sum of the squared residuals RSD as

$$\text{RSD} = \sum_{n=1}^{N} \left(s_{\text{fit}}(t_n; \tau_{\text{up}}, \tau_{\text{down}}, \tau_0, \delta_i) - n_{\text{exp}}(t_n)\right)^2, \tag{31}$$

where t_n is the sampling times of the oscilloscope and $n_{\text{exp}}(t_n)$ is the normalized experimental profile deduced through (29) and (30). By adjusting the parameter set $(\tau_{\text{up}}, \tau_{\text{down}}, \tau_0, \delta_i)$ through the MATLAB$^{\circledR}$'s function *fminsearch*, we can minimize RSD, which quantifies the difference between the theoretical profile and the experimental profile, and obtain the parameter set that better reproduces the data. From the τ values of this set, we compute τ_{tot} via (14). The scanning speed V_s (see (23)) is kept locked during the minimisation of RSD, its value being assigned as FSR/δt, where δt is the time interval needed to cross one FSR.

Figure 5 shows the results of the described fitting procedure when applied to a transfer signal and to a drop signal: it is worth noticing that the analysis is performed independently on the two channels, therefore the two τ_{tot} estimates are independent.

By repeating the fitting procedure on a series of resonances and treating statistically the resulting τ_{tot}'s, we obtain a final estimate in the form $\tau_{\text{tot}} = \hat{\tau} \pm \sigma_{\hat{\tau}}$, where

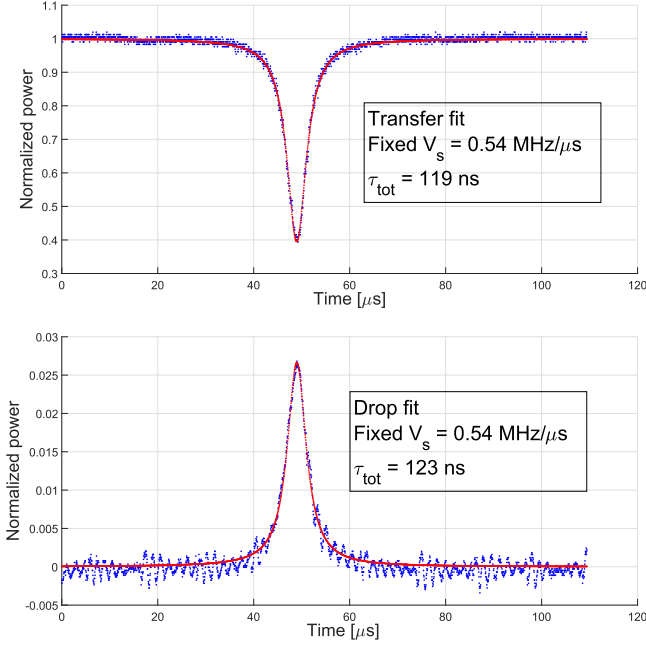$$\hat{\tau} = \sum_i^N \tau_{\text{tot}}^i \tag{32}$$

6

Figure 5. Typical data fitting results obtained through the minimisation of RSD. The red curves are the fitting profiles $s_{\text{fit}}^{\text{tra}}$ and $s_{\text{fit}}^{\text{drp}}$, while the blue curves are the normalized experimental profiles n_{tra} and n_{drp} from (29) and (30).

$$\sigma_{\hat{\tau}} = \sqrt{\sum_i^N \frac{(\hat{\tau} - \tau^i)^2}{N-1}} \qquad (33)$$

with τ_{tot}^i being the values resulting from data fitting and N being the number of analysed resonances (in our case $N = 13$). The dispersion of the τ_{tot}^i values can be caused by a combination of electric noise of the detectors and power instability of the laser source: in fact, both effects can affect the experimental profiles in an unpredictable way and produce shapes that yield different results under our analysis.

Finally, it is possible to switch the roles of the up-coupler and the down-coupler ('inverted configuration') and repeat the entire procedure to obtain two other independent estimates for τ_{tot}, reaching the total of four independent estimates, as reported in table 1.

3.3. Cavity ringdown analysis

In the case of CRD profiles, we propose an original analysis that uses transfer and drop profiles together to estimate the three lifetimes τ_0, τ_{up} and τ_{down}.

Initially, we focus on the transfer profile and define the quantity RSD_{tra} as:

$$\text{RSD}_{\text{tra}} = \sum_{n=1}^{N} (s_{\text{tra}}(t_n; V_s, \delta_i, \tau_0, \tau_{\text{up}}, \tau_{\text{down}}) - n_{\text{tra}}(t_n))^2$$

where s_{tra} is the theoretical profile (24) and n_{tra} is the normalized experimental profile (see (29)) and t_n are again the sampling times of the oscilloscope.

As for the stationary case, by minimisation of RSD_{tra} we can determine parameter set that better reproduces the data: in this case the adjusted parameters are the scanning speed V_s,

Table 1. Stationary regime results for the fiber ring resonator.

Configuration and analysed profile	$\tau_{\text{tot}} = \hat{\tau} \pm \sigma_{\hat{\tau}}$ (ns)
Direct transfer	116 ± 6
Direct drop	119 ± 12
Inverted transfer	118 ± 7
Inverted drop	120 ± 3

the initial detuning δ_i, the intrinsic lifetime τ_0 and the coupling lifetimes τ_{up} and τ_{down}. At the end of the minimisation procedure, however, only V_s, δ_i and τ_{up} are correctly estimated, while τ_0 and τ_{down} cannot be deemed trustful due to the exchange symmetry discussed in section 2.2.

To get τ_0 and τ_{down}, we need to analyse the drop profile, because these parameters appear in a non-symmetric way in (25) and the minimization algorithm can resolve their values. Therefore, we define RSD_{drp} as:

$$\text{RSD}_{\text{drp}} = \sum_{n=1}^{N} (s_{\text{drp}}(t_n; \{V_s, \delta_i, \tau_{\text{up}}\}_{\text{lock}}, \tau_0, \tau_{\text{down}}) - n_{\text{drp}}(t_n))^2$$

and minimize its value by adjusting only the values of τ_0 and τ_{down}, while keeping δ_i, V_s and τ_{up} locked to the values obtained from the first minimisation.

In the end, the values of δ_i, V_s and τ_{up} from the first minimisation and the values of τ_0 and τ_{down} from the second minimisation are our estimates for the entire parameter set $(V_s, \delta_i, \tau_0, \tau_{\text{up}}, \tau_{\text{down}})$. Figure 6 shows the typical results of the entire analysis procedure, having the fitting curves obtained through *fminsearch* in red and the normalized power profiles in blue.

As an additional verification of the consistency of the parameter set obtained through the two-step minimisation, we plot an additional green transfer curve ($s_{\text{tra}}^{\text{chk}}$) using these values and re-compute the residuals with respect to the experimental n_{tra} (RSD_{chk}), finding that the green curve is very close to the red curve and that the residuals RSD_{chk} are almost identical to the residuals RSD_{tra}.

By fitting a number of resonances, we can give a final estimate in the form $\tau = \hat{\tau} \pm \sigma_{\hat{\tau}}$ for each lifetime, following the same statistical method described in the previous section (see (33), $N = 17$ in this case). Then, from these estimates, we can compute τ_{tot} (see (14)) and deduce the values of $|k_{\text{up}}|^2$ and $|k_{\text{down}}|^2$ by inverting equations (11)–(13) and recalling that $\tau_{\text{rnd}} = 17$ ns.

The dispersion of τ's values can be related to the same effects we discussed during the stationary analysis, i.e. electric noise of the detectors and power fluctuations of the laser source, but also to the mathematical complexity of the fitting functions (24) and (25). In fact, due to this complexity, it is possible that *fminsearch* could converge in a region of relative minima close to the absolute minimum associated with the expected values. The evaluation of the contribution of each of these error sources to the τ's dispersion is a difficult task, therefore we treated the results with the statistical method described before, which estimates the overall dispersion.
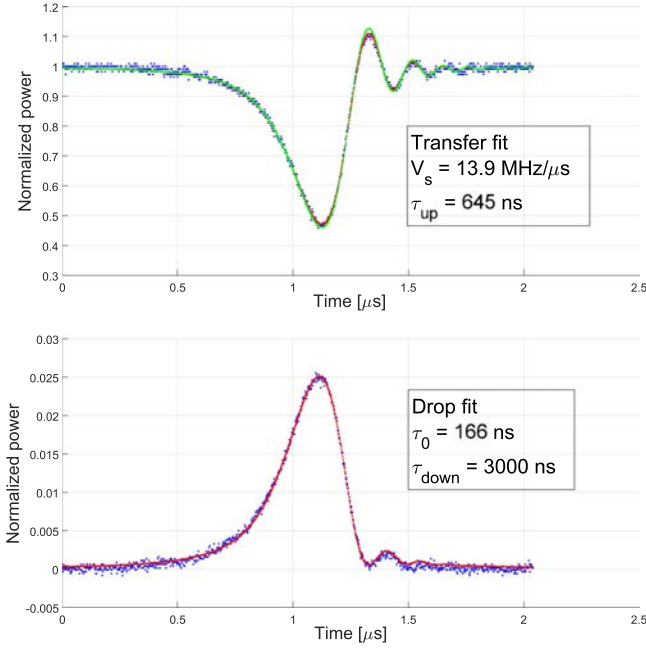
Figure 6. Typical results of the fitting procedure described in the main text. The red curves are the profiles obtained after the minimisation of RSD$_{tra}$ and RSD$_{drp}$, while the green profile is the consistency plot (s_{tra}^{chk}).

Table 2. CRD regime results for the fiber ring resonator.

	Direct conf.	Inverted conf.
τ_{tot} (ns)	120 ± 5	124 ± 4
$|k_{up}|^2$ (%)	4.99 ± 0.16	0.96 ± 0.06
$|k_{down}|^2$ (%)	1.16 ± 0.16	4.9 ± 0.3

As in section 3.2, we performed measurements in direct and inverted configurations: all results are shown in table 2. It is worth mentioning that, while comparing the results of the two configurations, the roles of the two couplers are exchanged and an *up*-parameter in one configuration has to be compared with the corresponding *down*-parameter in the other.

In the end, the presented analysis is able to reproduce the values of k_{up} and k_{down} found during the coupler character-isation, as well as to give τ_{tot} estimates consistent with the ones deduced from stationary measurement (see table 1): this means that our procedure is reliable and can be used to characterise an unknown resonator. We also notice that the characteristic lifetimes are determined with an accuracy that ranges from 3% to 8%.

4. Experiment with a WGM resonator

The analysis technique developed for the fiber ring resonator can be used to study the coupling of two tapered fibers with a high Q home-made WGM disk resonator. The resonator was fabricated in MgF$_2$ ($n = 1.37$) with the technique described in [31] and has a diameter $d_r = 3.83$ mm. This kind of study allows to deduce intrinsic properties of the resonator (like τ_0,
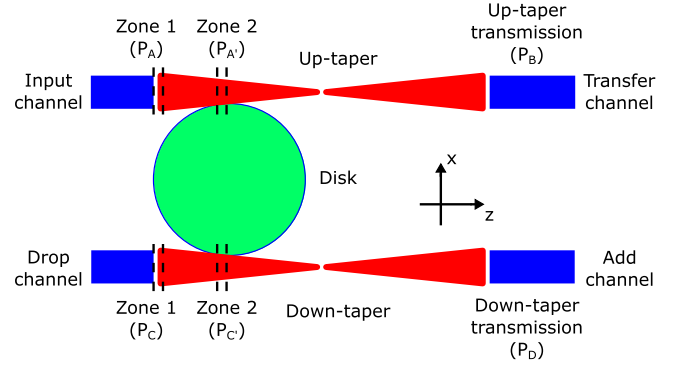

Figure 7. Relative position of the tapers and the disk after alignment: we marked with dashed lines the two coupling zones described in the main text. The figure is not intended to be in scale and the details are exaggerated for the sake of clarity.

η^2 and Q_0), as well as determining the strength of the coupling through $|k_{up}|^2$ and $|k_{down}|^2$: the knowledge of these parameters is extremely important when the WGM resonator is used in applications like sensing or filtering, or in basic studies like in the field of non-linear optics.

4.1. Setup description and data acquisition

For this experiment, we again used the setup shown in figure 4, with the resonator being the WGM crystalline disk (resonator B). In this case, light was coupled to the resonator through two home-made biconical tapered fibers [31], commonly addressed as *tapers* (red lines in figure 4). To move the two tapers and couple them to the disk, we used two independent translational stages with submicrometrical resolution along the three directions, while keeping the disk in a fixed position through an holder.

Positioning the biconical tapers was a critical part of the experiment in order to find the optimal configuration, as sketched in figure 7. While keeping the tapers in contact with the disk, we moved the up-taper from left to right in the disk equatorial plane and observed the transfer signal during a slow frequency scan, allowing us to find the region with the proper diameter to achieve good coupling (zone 2 in figure 7). From our estimates, zone 2 had a diameter around 4 μm and the taper was thick enough to assume no losses between zone 1 and zone 2 and we could assume $P_A = P_{A'}$. However, to the right of zone 2, losses could be present due to the diameter reduction: we could take them into account by measuring the powers P_B and P_A through an infrared power meter (Ando AQ2742) and defining the up-taper trans-mission factor $\gamma_{up} = P_B/P_{A'} = P_B/P_A$ (typically $\gamma_{up} \approx 90\%$). The entire procedure was then repeated to align the down-taper by putting the laser source on the drop channel and the drop detector on the add channel.

After both tapers had been aligned as shown in figure 7, the oscilloscope recorded, during a slow frequency scan, a series of dips for the transfer channel and a series of spikes for the drop channel. Differently from the fiber ring, we observed several different resonances (instead of the repetition of an identical one) and this is because the disk supports a great number of WGMs in the observed spectral interval (≈ 3 GHz), each characterised with its own resonant
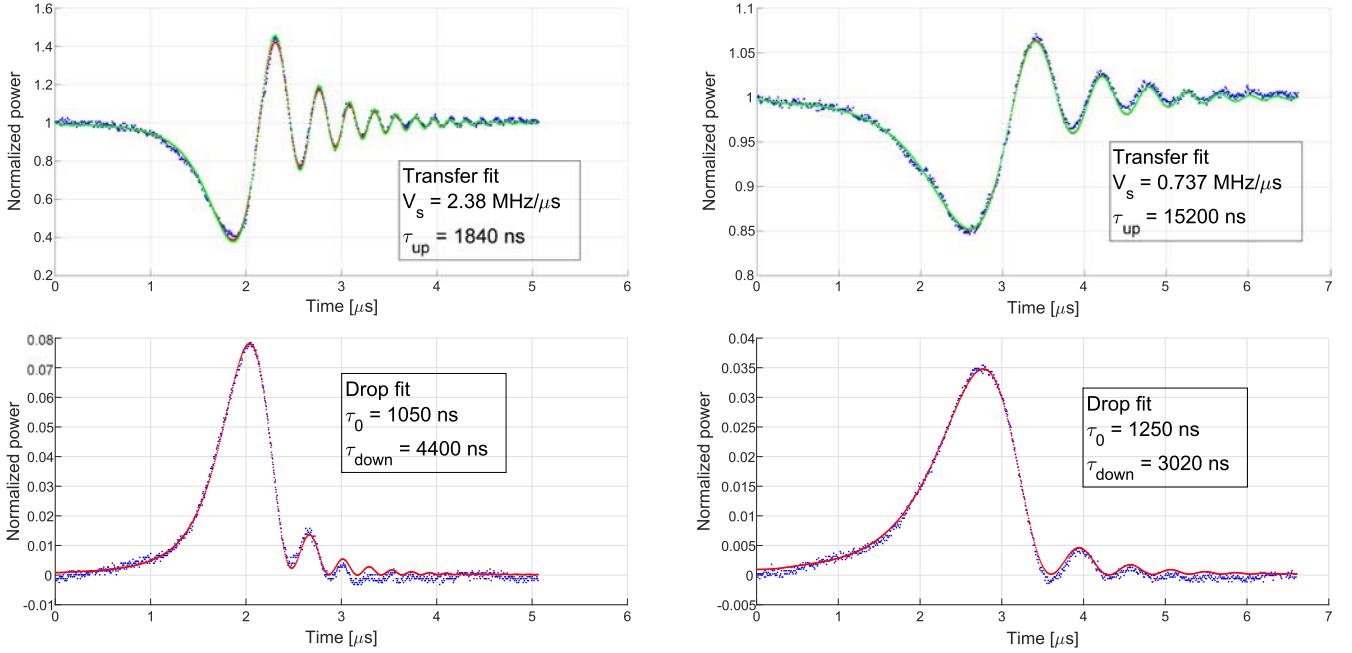
Figure 8. Transfer and drop profiles for two typical CRD resonances (A on the left and B on the right). The figure reports the normalized experimental profile in blue, the fitting curve in the red and the consistency curve in the green; it also shows the τ's values, while the complete numerical results are listed in table 3. The two resonances are obtained for different scanning speeds and coupling conditions.

frequency, its own (k_{up}, k_{down}) set and its own quality factor Q_{tot} [28].

Once we selected the resonance to study, we maximized its contrast using the polarisation controller and then increased the scanning speed V_s, switching to the CRD regime. The acquired CRD profiles undergo the same normalisation procedure described in section 3.1 and therefore we have

$$P_{tra} = P_{A'} = \frac{P_B}{\gamma_{up}} = \frac{a_{tra}(V_{det,tra} - q_{tra})}{m_{tra}\,\gamma_{up}}$$

$$P_{drp} = P_{C'} = P_C = \frac{(V_{det,drp} - q_{drp})}{m_{drp}}$$

$$n_{tra} = \frac{P_{tra}}{P_{in}} \qquad \text{and} \qquad n_{drp} = \frac{P_{drp}}{P_{in}},$$

where P_{in} is again the out-of-resonance optical power deduced by the power signal P_{tra}.

4.2. Data analysis

From the normalized profiles, it is possible to deduce the lifetimes τ_{up}, τ_{down} and τ_0 using the fitting procedure validated in section 3 on the fiber ring resonator. As previously noted, for the disk resonator each resonance is physically different, corresponding to one of the several WGMs that can be excited and being characterised by its own set of parameters: figure 8 shows the results for two typical resonances, labelled as A (left side) and B (right side). Similarly to the case of the fiber ring resonator, the figure reports the normalized experimental profile in blue, the fitting curve in red and the consistency curve in green: the two resonances are obtained for different scanning speeds and coupling conditions.

Since the observed spectral window was less than the disk FSR (≈ 18 GHz), we cannot analyse replicas of A and B to deduce the experimental error with the statistical method seen in section 3 (see (33)) and we cannot estimate directly the errors on the τ's and the other parameters of the WGM resonator. Therefore, in reporting these quantities in table 3, we decide to round the numbers to two significant digits, in analogy with table 2.

Even if the disk resonances appear similar to the ones of the fiber ring resonator, the values of the parameters are very different. In fact, the intrinsic losses (η^2) and the coupling losses ($|k_{up}|^2$ and $|k_{down}|^2$) have a magnitude of 10^{-5} or 10^{-6}, meaning that very little light is lost by or coupled into the resonator. The Q's have very high values, typically around 10^8 and 10^9, with the intrinsic quality factors Q_0's close to the state-of-the-art values.

However, for practical applications like sensing and non linear optics studies, the most important parameter is the finesse $\mathcal{F}$, which is a measure of the average number of round trip performed by a photon inside the resonator before being lost.

Together with the finesse $\mathcal{F}$, it is usual to define the intrinsic finesse $\mathcal{F}_0$, which takes into account only the intrinsic losses, just as the intrinsic quality factor Q_0:

$$\mathcal{F}_0 = \frac{\pi\,\tau_0}{\tau_{rnd}} = Q_0\,\frac{FSR}{\nu_0}, \qquad (34)$$

where ν_0 is the resonance frequency. The intrinsic finesse $\mathcal{F}_0$ is reported in table 3 along with the other parameters. In particular, for resonance B we have obtained the highest values of $Q_0 = 7.5 \cdot 10^8$ and $\mathcal{F}_0 = 7.2 \cdot 10^4$.

Since the two resonances A and B correspond to different WGMs, we expect the modes to have different geometries,

Table 3. Analysis results for the WGM resonances 'A' and 'B' from figure 8.

	Resonance A	Resonance B
τ_0 (ns)	1000	1300
τ_{up} (ns)	1800	15000
τ_{down} (ns)	4400	3000
τ_{tot} (ns)	580	840
η^2	$10 \cdot 10^{-5}$	$8.8 \cdot 10^{-5}$
$|k_{\text{up}}|^2$	$6.0 \cdot 10^{-5}$	$0.73 \cdot 10^{-5}$
$|k_{\text{down}}|^2$	$2.5 \cdot 10^{-5}$	$3.6 \cdot 10^{-5}$
Q_0	$6.3 \cdot 10^8$	$7.5 \cdot 10^8$
Q_{up}	$11 \cdot 10^8$	$91 \cdot 10^8$
Q_{down}	$26 \cdot 10^8$	$18 \cdot 10^8$
Q_{tot}	$3.5 \cdot 10^8$	$5.0 \cdot 10^8$
$\mathcal{F}$	$3.3 \cdot 10^4$	$4.8 \cdot 10^4$
$\mathcal{F}_0$	$6.0 \cdot 10^4$	$7.2 \cdot 10^4$

producing different coupling factors $|k_{\text{up}}|^2$ and $|k_{\text{down}}|^2$: this is confirmed by the numerical results of table 3. The small difference in η^2 and τ_0 can be explained by the difference in the mode geometry and taking into account the fact that the intrinsic losses are mostly due to surface imperfections. In fact, since the two modes touch the surface in different points with their evanescent tails and the resonator surface is not perfectly homogeneous, the surface losses for the two modes can be slightly different.

5. Conclusions

In this work, we have studied a ring resonator in the add-drop configuration, which is a common configuration in applied optics as well as in some fundamental studies involving high-Q WGM resonators. In all these cases, the deduction of the intrinsic properties of the resonator and its interaction with the coupling waveguides is a fundamental aspect.

The standard analysis method, which is based on the data fitting of stationary profiles, proved to be not sufficient for this purpose, and therefore we investigated a different approach, studying the CRD regime, which allowed us to fully characterise the system. We developed a theoretical model describing both the transfer and drop signals, starting from the known solution of the single coupler case found in literature, and then set up the experiment to check the validity of the model.

The theoretical model predicted well the experimental CRD profiles for both transfer and drop channels and we developed an original fitting procedure to deduce the parameters characterising the resonator. The analysis method was tested with an experiment on a fiber ring resonator of known characteristics. The expected values were well reproduced and the error on these estimates, deduced by a statistical analysis, were equal to a few percentage points.

The validated analysis method, which was developed to be general and independent from the specific type of resonator, was then used to characterise a high Q WGM disk resonator. From a simultaneous acquisition of the transfer and drop signals, we could assess the main parameters of the resonator and its coupling to the waveguides, achieving the main goal of this work.

We also envisage an addition to the theoretical model developed in this work, so that it can take into account the possibility of selective amplification (negative lifetime τ_0 [32]) and coupling between two resonators [33].

ORCID iDs

G Frigenti ⓘ https://orcid.org/0000-0002-4290-3158
M Arjmand ⓘ https://orcid.org/0000-0001-9993-4767
Y Dumeige ⓘ https://orcid.org/0000-0001-9003-0809

References

[1] Chiasera A, Dumeige Y, Féron P, Ferrari M, Jestin Y, Conti G N, Pelli S, Soria S and Righini G 2010 *Laser Photonics Rev.* **4** 457
[2] Guo H, Karpov M, Lucas E, Kordts A, Pfeiffer M H P, Brasch V, Lihachev G, Lobanov V E, Gorodetsky M L and Kippenberg T J 2017 *Nat. Phys.* **13** 94
[3] Liang W, Eliyahu D, Ilchenko V S, Savchenkov A A, Matsko A B, Seidel D and Maleki L 2015 *Nat. Commun.* **6** 7957
[4] Wang C Y, Herr T, Del'Haye P, Schliesser A, Hofer J, Holzwarth R, Hänsch T W, Picqué N and Kippenberg T J 2013 *Nat. Commun.* **4** 1345
[5] Kippenberg T J, Holzwarth R and Diddams S A 2011 *Science* **332** 555
[6] Farnesi D, Barucci A, Righini G, Berneschi S, Soria S and Conti G N 2014 *Phys. Rev. Lett.* **112** 093901
[7] Farnesi D, Barucci A, Righini G, Conti G N and Soria S 2015 *Opt. Lett.* **40** 4508
[8] Farnesi D, Righini G, Conti G N and Soria S 2017 *Sci. Rep.* **7** 44198
[9] Farnesi D, Berneschi S, Cosi F, Righini G C, Soria S and Conti G N 2016 *J. Vis. Exp.* **110** e53938
[10] de Cumis M S *et al* 2016 *Laser Photon Rev.* **10** 153

[11] Fescenko I, Alnis J, Schliesser A, Wang C Y, Kippenberg T J and Hänsch T W 2012 *Opt. Express* **20** 19185

[12] Liang W, Ilchenko V S, Savchenkov A A, Matsko A B, Seidel D and Maleki L 2010 *Opt. Lett.* **35** 2822

[13] Peccianti M, Pasquazi A, Park Y, Little B, Chu S, Moss D and Morandotti R 2012 *Nat. Commun.* **3** 765

[14] Ristic D *et al* 2016 *J. Lumin.* **170** 755

[15] Yao X S and Maleki L 1996 *J. Opt. Soc. Am.* B **13** 1725

[16] Liang W, Eliyahu D, Ilchenko V S, Savchenkov A A, Matsko A B, Seidel D and Maleki L 2015 *Nat. Commun.* **6** 7957

[17] Monifi F, Friedlein J, Özmedir Ş K and Yang L 2012 *J. Lightwave Technol.* **30** 3306

[18] Razdolskiy I, Berneschi S, Conti G N, Pelli S, Murzina T V, Righini G C and Soria S 2011 *Opt. Express* **19** 9523

[19] Roy S, Prasad M, Topolancik J and Vollmer F 2010 *J. Appl. Phys.* **107** 053115

[20] Poellinger M and Rauschenbeutel A 2010 *Opt. Express* **18** 17764

[21] Razdolskiy I, Berneschi S, Conti G N, Pelli S, Murzina T V, Righini G C and Soria S 2011 *Opt. Express* **19** 9523

[22] Yang Y, Madugani R, Kasumie S, Ward J M and Chormaic S N 2016 *Appl. Phys.* B **122** 291

[23] Giorgini A, Avino S, Malara P, Natale P D and Gagliardi G 2017 *Sci. Rep.* **7** 41997

[24] Chen L, Liu Q, Zhang W G and Chou K C 2016 *Sci. Rep.* **6** 38922

[25] Dumeige Y, Trebaol S, Ghişa L, Nguyên T, Tavernier H and Féron P 2008 *J. Opt. Soc. Am.* B **25** 2073

[26] Gorodetsky M L and Ilchenko V S 1999 *J. Opt. Soc. Am.* B **16** 147

[27] Yariv A 2000 *Electron. Lett.* **36** 321

[28] Little B E, Laine J P and Haus H A 1999 *J. Lightwave Technol.* **17** 704

[29] Matsko A and Ilchenko V 2006 *IEEE J. Sel. Top. Quantum Electron.* **12** 3

[30] Haus H A 1984 *Waves and Fields in Optoelectronics* (Englewood Cliffs, NJ: Prentice-Hall) ch 7

[31] Merrer P H, Saleh K, Llopis O, Berneschi S, Cosi F and Conti G N 2012 *Appl. Opt.* **51** 4742

[32] Rasoloniaina A, Huet V, Nguyên T K N, Cren E L, Mortier M, Michely L, Dumeige Y and Féron P 2014 *Sci. Rep.* **4** 4023

[33] Rasoloniaina A, Huet V, Thual M, Balac S, Féron P and Dumeige Y 2015 *J. Opt. Soc. Am.* B **32** 370